The Journal of Undergraduate Research in Physics

CONTENTS

VOLUME 1, NUMBER 2

OCTOBER, 1982

Published by Guilford College
for
The American Institute of Physics and The Society of Physics Students

THE JOURNAL OF UNDERGRADUATE RESEARCH IN PHYSICS

This journal is devoted to research work done by undergraduate students in physics and its related fields. It is to be a vehicle for the exchange of ideas and information by undergraduate students. Information for students wishing to submit manuscripts for possible inclusion in the Journal follows.

ELIGIBILITY

The author must have performed all work reported in the paper as an undergraduate. The subject matter of the paper is open to any area of pure or applied physics or physics related field.

SPONSORSHIP

Each paper must be sponsored by a full-time faculty member of the department in which the research was done. The name, address, and phone number of the sponsoring faculty member must be included with the manuscript.

FORM

The manuscript should be typed, double spaced, on 8 1/2 x 11 inch sheets. Margins of about 1 1/2 inch should be left on the top, sides, and bottom of each page. Papers should be limited to twelve pages of text in addition to an abstract and appropriate drawings, pictures, and tables.

GENERAL STYLE

All papers must conform to the Style Manual of the American Institute of Physics. Each paper must be prefaced by an abstract that does not exceed 250 words.

ILLUSTRATIONS

Line drawings should be made with black India ink on plain white paper. If a graph is drawn on co-ordinate paper, the paper must be lined blue. Important lines should be ruled in black. Each figure or table must be on a separate sheet. Photographs must have a high gloss finish.

CAPTIONS

A brief caption should be provided for each illustration or table, but it should not be part of the figure. They should be listed together at the end of the manuscript.

EQUATIONS

Equations should appear on separate lines and may be written in black India ink.

FOOTNOTES

Footnotes should be typed double spaced and grouped together in sequence at the end of the manuscript.

SUBMISSION

Two copies of the manuscript should be sent to:

Dr. Rexford E. Adelberger, Editor
THE JOURNAL OF UNDERGRADUATE RESEARCH IN PHYSICS
Physics Department
Guilford College
Greensboro, NC 27410

SUBSCRIPTION INFORMATION

The Journal will be published biannually with issues appearing in April and October of each year. There will be two issues per volume.

TYPE OF SUBSCRIBER	PRICE PER VOLUME
Individual	$ 5.00
Institution	$10.00

Foreign subscribers add $2.00 for postage

To receive a subscription, send your name, address, and check made out to The Journal of Undergraduate Research in Physics to:

Journal of Undergraduate Research in Physics
Physics Department
Guilford College
Greensboro, NC 27410

ISSN 0731 - 3764

The Journal of Undergraduate Research in Physics is published by Guilford College for the American Insititute of Physics and the Society of Physics Students.

EVIDENCE FOR A MICROTUBULE-ASSOCIATED MAGNETIC FIELD

William J. Meikrantz
Department of Physics
Guilford College, Greensboro, NC 27410

ABSTRACT

The charge flux due to GTP hydrolysis down the helical length of labile or polmerizing microtubules suggests that they possess an intrinsic magnetic field. An attempt is made to establish the presence of this field employing the Gouy balance method, using suspensions of Tetrahymena pyriformis as well as a Tetrahymena-derived cell-free system. These samples did indeed display a net magnetization, apparently ferromagnetic in character, that was dependent upon cell concentration, applied field strength, and that was altered by the presence of colchicine.

INTRODUCTION

Microtubules (hereafter abbreviated Mts) are the basic components of eukaryotes from which larger structures concerned with cell shape or movement (such as the spindle fibers or cilia and flagella in protozoans) are constructed. (1) Mts are built up from smaller protofilaments (usually thirteen) arranged longitudinally to form hollow cylinders about 25 nm in diameter. The protofilament is a stable entity built up from dimers of tubulin, a protein consisting of two subunits of smaller size (the α and β subunits), into a helix about 4 nm in diameter with repeat length of about 8 nm.

Kinetic (2) and thermodynamic (3) analyses of Mt assembly, further supported by microscopic observation (4), indicate the so-called "condensation mechanism" (5) of Mt assembly, according to which polymerization takes place by the addition of a tubulin subunit to the end of the Mt, the addition of a single dimer being the rate-limiting step. It is further found (6) that one GTP (guanine nucleoside triphosphate) molecule is hydrolyzed to GDP (guanine nucleoside diphosphate) for each subunit added, the guanine nucleotide being tightly bound to the subunit. It is also apparent that addition (and removal) of subunits occurs at both ends of the Mt (7); however, due to an inherent polarity in the Mt, the net rate of addition is greatest at one end, (8) the other usually being capped or anchored in vivo.

The result of the chemical coupling of GTP hydrolysis to Mt assembly is not known. This hydrolysis does not provide the energy for assembly, as tubulin readily polymerizes in the presence of nonhydrolyzable analogues of GTP (9). In a discussion based on microfilament assembly (from actin subunits coupled to ATP hydrolysis), Wegner has described the hydrolysis of the nucleoside triphosphate coupled with the known polarity of the subunits as leading to net polymerization at one end of the polymer and net depolymerization at the other, under steady-state conditions. (10) Margolis and Wilson have demonstrated that there is a rapid exchange of free subunits with tubulin polymers at steady-state in vitro. (11) In vivo, however, it is not clear that such "treadmilling" could take place among capped or anchored filaments. Kirschner has recently suggested (12) that GTP hydrolysis may serve to produce a disparity in the critical concentration of tubulin subunits needed at the two ends of the polymer, leading to treadmilling in vitro and to suppression of spontaneous polymerization in vivo. These treatments are questionable, however, as both discussions assume the polymerization reaction to be reversible, whereas the dissociation of intact Mts into subunits bound to GTP has not been observed (i.e., phosphorylation of subunit GDP upon dissociation does not appear to take place).

In this paper, evidence for a direct physical consequence of assembly-coupled GTP hydrolysis is presented. The charge flux due to GTP hydrolysis down the length of polymerizing Mts ought to lead to a magnetic field oriented in the direction of the polymerization, of magnitude

$$\mu \, i \, N / 2L$$

where i is the GTP→ GDP "current" and N is the number of turns in the length L of the helix. This is on the order of 1 pico-Gauss for a Mt 10 microns long. It should be noted that this magnetic field is only a result of the presence of the charge flux, and is thus present only when a) the polymer is in the process of assembling, or b) when the assembled Mt is in equilibrium with a pool of tubulin

subunits (which is the case in vivo). Stable (i.e., ciliary or flagellar) Mts will not possess an intrinsic magnetic field, while the labile Mts of the cytoplasm will. We may therefore expect suspensions of Mts or Mt-containing cells to behave analogously to paramagnetic solutions when placed in an external magnetic field. We may also expect any detected magnetic effect to be disrupted by typical Mt inhibitors (13), such as the alkaloid colchicine used in this investigation.

MATERIALS AND METHODS

Cell culture

The cells used in this investigation were Tetrahymena pyriformis (hereafter abbreviated TH) obtained from the Biology Department at Guilford College. The TH were grown in a defined growth medium (14) (hereafter abbreviated DGM) at a constant temperature of 27 C.

Cell-free system

A cell-free system (CFS) derived from TH was prepared by homogenization of TH in DGM using a Teflon-pestle homogenizer. The cell homogenate was centrifuged in a clinical centrifuge for 1 hr to remove membrane debris. The supernatant was mixed with an equal volume of 0.1 M Mes (2-(N-Morpholino) ethanesulfonic acid) buffer: (15) 0.1 M Mes, 1 mM EGTA - Ethylene bis(oxyethylenenitrilo) -tetraacetic acid), 1 mM GTP, 0.5 mM MgCl, at pH 6.4. The CFS was stored at 0 C, thawed in a refrigerator before use, and kept for no longer than 8 hrs.

The Gouy balance

If a sample of a paramagnetic substance is suspended vertically such that it partially lies within a horizontal magnetic field, it experiences a downward force F of magnitude

$$F = -\chi A H/2$$

where A is the cross-sectional area of the sample, χ is the volume magnetic susceptibility, and H is the strength of the applied field. In the Gouy balance method (16), the sample is suspended so that it hangs partially within a homogeneous magnetic field. As the field strength is increased, the force on the sample due to the field can be read directly from the balance. The apparatus used in this investigation is drawn schematically in Figure 1. The balance used was a Mettler Type H6 readable to 0.1 mg. The samples were housed in thin-walled Pyrex NMR tubes 18 cm long x 0.5 cm diameter. Sample volumes of 2 ml were used, with care taken to avoid the formation of air bubbles during preparation. The samples were suspended with copper wire so that 1 cm of the sample hung in the region between the pole faces. Since this investigation was principally qualitative, no attempt was made to calibrate the samples with substances of known susceptibility.

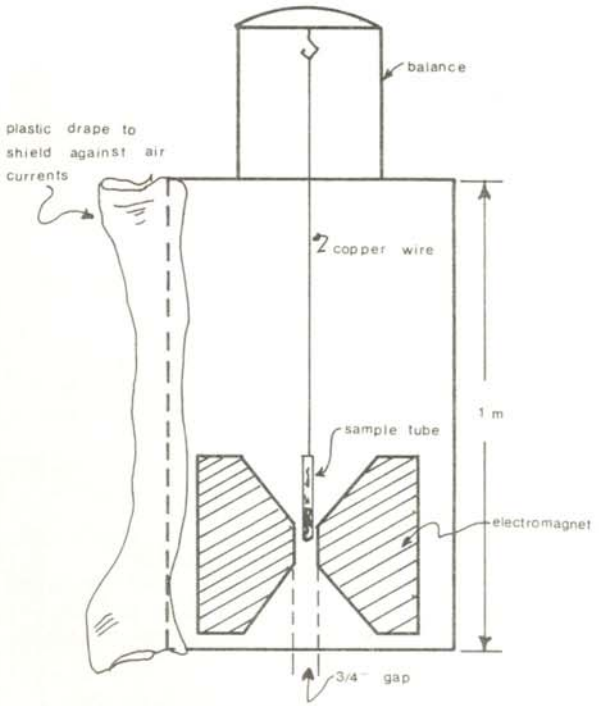

FIGURE 1
Diagram of the Gouy balance apparatus

Experimental design

Three sets of measurements were carried out: a) the same sample of cells was subjected to a field increasing from 0 to 5 KGauss at 1 KGauss intervals. This is called the magnetic survey of the sample. b)Successive dilutions of cell samples were subjected to a constant field of 3 KGauss. c) Suspensions of TH into which increasing amounts of 1 μM colchicine had been introduced were subjected to a constant field of 3 KGauss. For each set of measurements, the initial weights of all samples were normalized to the same value to facilitate comparison.

Preparation of TH concentrations

0.6 ml, 0.8 ml, 1.0 ml, 1.2 ml,... 2.0 ml of TH in DGM from the parent culture (a highly dense concentration of TH) were added to culture tubes containing 5 ml DGM, from which 2 ml samples were taken for measurement.

Preparation of colchicine concentrations

To five culture tubes containing 5 ml DGM inoculated with 2 ml of TH in DGM from the parent flask were added 5, 10, 15, 20, 25 drops (0.05 ml) of 1μM colchicine. Samples of 2 ml were taken for measurements.

Preparation of blanks

For each sample tube prepared, a blank was made up containing everything but TH in the same proportion. CFS blanks contained 2 ml of a 1:1 mixture of DGM and 0.1 M Mes. The initial weights of the blanks were normalized to the same values as the sample tubes in each experiment. The use of blanks prepared in this manner allows effects due to the glass of the tubes, the suspension media, or the presence of colchicine to be subtracted out directly.

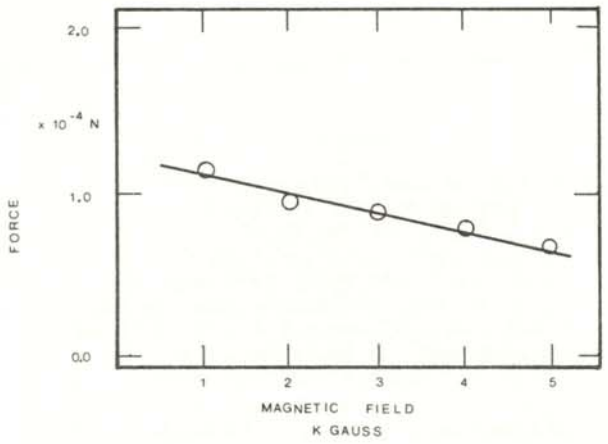

FIGURE 2
Magnetic survey of TH

RESULTS

Effect of colchicine on TH and CFS preparations

The Mt activity of the TH and CFS preparations was determined by measuring the absorbance of these systems at a wavelength of 520 nm. Assembled (intact) Mts absorb strongly at 520 nm, thus addition of colchicine should cause a decrease in absorption for the two systems. This was indeed found to be the case. Increasing amounts of 1 μM colchicine were added to 2 ml samples each of TH and the CFS; the absorption at 520 nm was measured against blanks containing 2 ml DGM for the TH suspension and 2 ml DGM + Mes (1:1) for the CFS plus the same amount colchicine as was added to the samples.

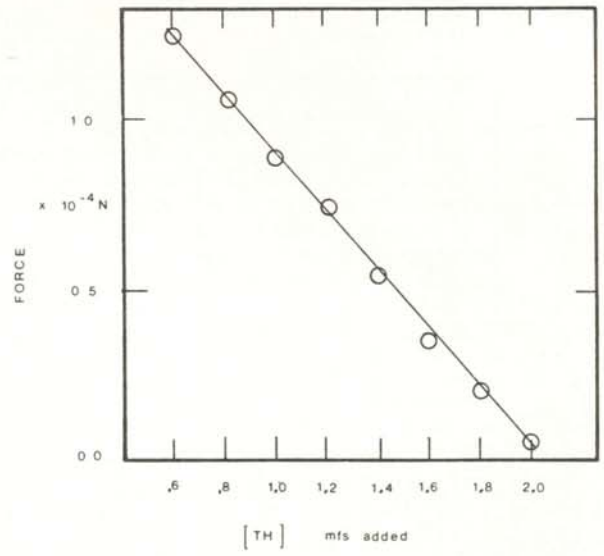

FIGURE 3
Effect of varying cell concentration with constant applied field.

Magnetic survey of TH suspension

These results appear in Figure 2. Note that instead of a pure paramagnetic effect, there is a strong diamagnetic background. This is not due to the glass sample tube or the suspension medium, as the forces on these are subtracted out via the blank. The overall trend, however, is of decreasing repulsive force, and thus increasing attractive force which is due to the presence of the TH.

Effect of cell concentration with constant field

These results appear in Figure 3. The diamagnetic background persists, but the general trend is of increasing attraction, which is proportional to the increasing cell concentration.

Effect of colchicine

These results appear in Figure 4 and are discussed specifically below.

DISCUSSION

Analysis of error

The standard deviation for all force measurements derived from repetition of the experiments is $\sigma = \pm 5$ μN. Differences in force due to differences in composition of the sample tubes yields an additional error of 5 μN resulting in a total uncertainty in the force measurements of 0.7 μN.

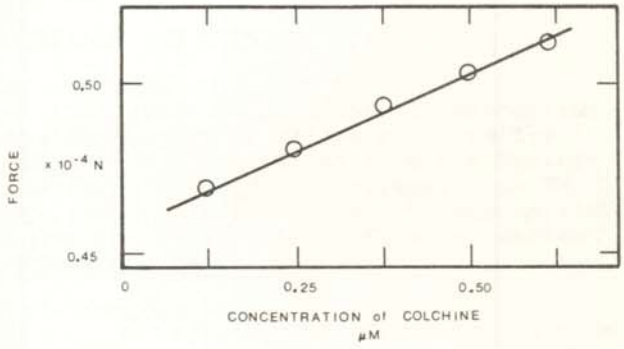

FIGURE 4
Effect of varying concentrations of colchicine added to TH with constant applied field.

Source of the diamagnetic background

The source of the diamagnetic background, since it does not come from either the sample tube or suspension medium, must result from part of the cell itself. The cell membrane is the logical candidate for the diamagnetic source for several reasons: a) it completely encloses the labile Mts; thus they generate a magnetic flux across the membrane, b) the (often charged) protein and lipid components of the membrane are relatively free to move about around the membrane, and c) Mts are suspected to interact with membrane-associated proteins. (17) A TH-derived CFS was prepared as described above and subjected to the magnetic survey (along with the corresponding blank). These results appear in Figure 5. The effect is purely attractive; the attractive force (-F) increases constantly with the applied field. To make sure that the force was due to Mts and was not artefactual or caused by some other cell component, the survey was repeated with 0.5 ml of 1 μM colchicine added to the 2 ml sample and its blank. The attractive force is damped out significantly (to within one standard deviation of zero; hence these data are not shown on the graph), so the hypothesis is confirmed. The total uncertainty in F is ± 7 μN which includes the sample tube error and the standard deviation of the measurements.

Linear dependence of F on H

The theoretical equation for the force in the Gouy balance method is

$$-\chi_m A H/2$$

as stated above. The derivation of this result from the energy of magnetization depends on two assumptions: linear magnetization of the sample and zero initial magnetization. These characteristics are typical of true paramagnetic materials, stemming from the fact that atomic and molecular moments giving rise to net magnetization do not strongly interact with each other, due to the disorienting effect of Brownian motion. Here, however, we are concerned with structures not easily disturbed by the Brownian movement because of their large mass. Support for the ferromagnetic character of the interaction is found in Figure 3. If the diamagnetic effect is due to the membrane, then F should be directly rather than inversely proportional to the number of cells

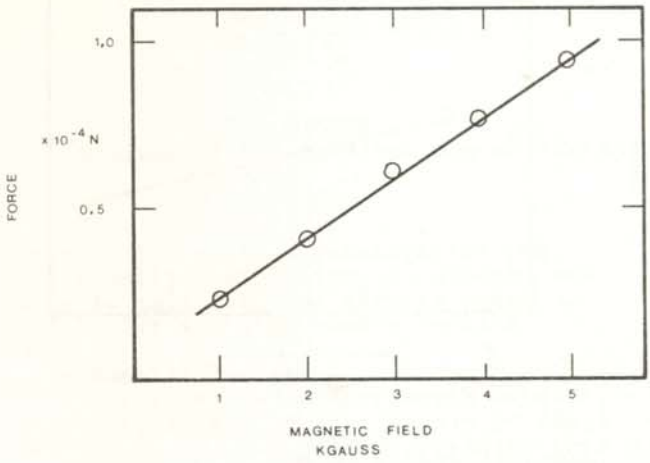

FIGURE 5
Magnetic survey of the cell free system.

present. Increasing the cell concentration, however, would increase the likelihood of cell-cell (domain-domain) interactions, resulting in a continuing dominance of the attractive force over the repulsive force due to mutual alignment of domains. This proposal must remain

tentative pending estimation of actual domain size. In addition, it was found that, after returning the applied field to zero, the force on the various samples did not return to its original value (data not presented). This hysteresis effect is also uniquely characteristic of ferromagnetic materials.

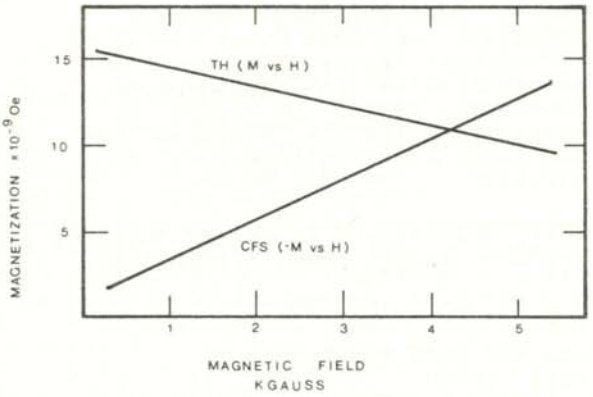

FIGURE 6
Magnetization of CFS and TH.

The force equation may be written in the more general form

$$-\chi AHB/2 = -AHM/2$$

where B is the effective field as opposed to the applied field H, and M is the magnetization χB, which is graphed for the TH and CFS in Figure 6. Several factors are apparent from the figure: a) The energy of magnetization per volume (for the CFS, U = 2.8 pico Joules, for TH, U = 1.5 pico Joules), and b) the dominant term in the expression for the magnetization is the initial magnetization, indicating that a broader range of applied field values is needed for a more accurate characterization of the magnetization of the samples.

Effect of colchicine on intact TM

The results presented in Figure 4 are somewhat ambiguous. There is a slight increase in repulsive force, which is to be expected as the Mts are depolymerized, but the addition of colchicine seems to have increased the attractive force from its original value (cf. Figure 2). In the light of the results obtained from the CFS, it is tempting to hypothesize that the colchicine concentration used was too small. This would indeed produce only a slight increase in the repulsive force, but without completely depolymerizing all the Mts. Since the field of a single Mt is only proportional to the coils per length in its helix, the net result would be an increase in attractive force due to the greater number of shorter Mts present which remain in equilibrium with the cytoplasmic pool of free tubulin. The amount of free tubulin would also be reduced to stoichiometric binding to colchicine. This wold be consistent with the absorption data obtained previously.

CONCLUSION

It has been shown that a) TH produce a ferromagnetic effect when placed in an external magnetic field, b) the magnitude of this effect is linearly proportional to the concentration of TH present, c) the effect is altered by the presence of colchicine, d) the effect occurs in semi-purified preparations of Mts (i.e., in TH-derived CFS) and that there, the effect is significantly inhibited by colchicine. Further research with purified tubulin preparations over a broader range of applied field strengths is called for. Three components of the effect need to be investigated carefully: the character of the charge flux, the nature of the magnetization, and the diamagnetic effect linked to the membrane.

It is interesting to speculate what purpose a Mt-associated magnetic field might play in the cell. The only other molecule known to be coupled to a charge flux during its formation is DNA. Here, however, it is not clear whether a magnetic field would result due to enzyme-substrate interactions and supercoiling. In the spindle, Mts are known to bear dynein cross-links. Dynein is an ATPase similar to the F1-ATPase which in mitochondria is driven by an electromotive force. The vectoral orientation of the dynein arms in the spindle, orthogonal to the Mts, becomes quite provocative when considered in the light of recent proposals (17) concerning the cause of chromosome segregation during cell division.

REFERENCES

(1) See B. Lewin, Gene Expression (Vol II: Eukaryotic Chromosomes), New York: Wiley-Interscience, 1980 for a review of Mt structure and function.

(2) K.A. Johnson and G.G. Borisy, J. Mol. Biol. (1977) 117:1-31

(3) K.A. Johnson and G.G. Borisy, J. Mol. Biol. (1979) 133:199-216

(4) L.G. Bergen and G.G. Borisy, J. Cell Biol. (1980) 84:141-150., S.R. Heidemann, G.W. Zieve, and J.R. McIntosh, J. Cell Biol. (1980) 87:152-163., K. Summers and M.W. Kirschner, J. Cell Biol. (1979) 83:204-217.

(5) F. Gaskin, C.R. Cantor, and M.L. Shelanski, J. Mol. Biol. (1974) 89:737-758, F. Cosawa and M. Kasai, J. Mol. Biol. (1962) 4:10-21.

(6) Lewin, op.cit. p.21.

(7) R.L. Margolis and L. Wilson, Cell (1978) 13:1-8.

(8) Bergen and Borisy, ibid.

(9) See for example T. Arai and Y. Kaziro, Biochem. Biophys. Res. Comm. (1976) 69:369-376.

(10) A. Wegner, J. Mol. Biol. (1976) 108: 139-150.

(11) Margolis and Wilson, ibid.

(12) M. Kirschner, J. Cell Biol. (1980) 86:330-334.

(13) Lewin, op. cit. pp.30-38.

(14) G.W. Kidder and V.C. Dewey in Vol I: Biochemistry and Physiology of Protozoa, A. Lwoff, ed., New York: Academic Press, P. 324. (1951).

(15) R.C. Weisenberg, Science (1972) 177:1104-1105.

(16) For a recent review of the Gouy technique, see L.N. Mulay (1972). "Techniques for measuring magnetic susceptibility" in Techniques of Chemistry, Part IV of Vol IA, A. Weissberger and B.W. Rossiter, eds. New York: Wiley-Interscience, pp. 431-453.

(17) J.R.. McIntosh, P.K. Helper, and D.G. Van Wie, Nature (1969) 224:659-663.

SPONSORS FOR THIS PAPER
Dr. Frank Keegan
Department of Biology
Guilford College, Greensboro, NC. 27410

Dr. Rexford Adelberger
Department of Physics
Guilford College, Greensboro, NC. 27410

ABERRATION OF A PLANO-CONCAVE LENS HAVING A PARABOLIC SURFACE

Walter S. Allensworth
Physics Department
Wofford College, Spartanburg, SC 29301

ABSTRACT

Using ray tracing, the longitudinal parabolic aberration of a plano-concave parabolic lens is determined exactly. Both theoretical and experimental data are presented and compared. This aberration can be interpreted by comparison with the fifth-order longitudinal spherical aberration for lenses having spherical surfaces.

INTRODUCTION

A lens having a paraboloid of revolution and a plane as the two refracting surfaces has been found to exhibit a longitudinal parabolic aberration which has several interesting properties. Among these are that the image distance can be expressed in closed form without approximation, that the sign of the aberration can be both positive and negative for the same lens, that the functional form is similar to the fifth-order effect for spherical lenses, and that the magnitude of this aberration can be quite large.

THEORY

In the case of lenses with spherical surfaces, the longitudinal spherical aberration (LSA) is defined by (1)

$$LSA = Sp - Sh, \qquad (1)$$

where Sp is the image distance for paraxial rays and Sh is the image distance for a ray of ray-height h. For the

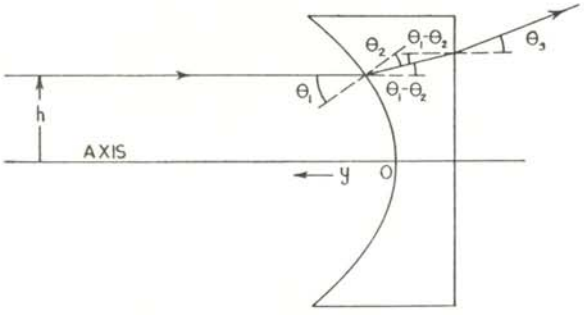

FIGURE 1
Ray diagram showing the refractions at the two surfaces of the plano-concave lens having a parabolic surface.

parabolic lens under consideration, the longitudinal parabolic aberration (LPA) will be defined in the same way

$$LPA = Sp - Sh. \qquad (2)$$

The LPA can be determined by ray tracing. As shown in Figure 1, the angle of refraction at the parabolic surface is, by Snell's law,

$$\theta 2 = \arcsin((\sin \theta 1)/n), \qquad (3)$$

where n is the index of refraction of the lens. The angle of incidence for the second refraction is $\theta 1 - \theta 2$. Snell's law then gives the angle of refraction at the plane surface as

$$\theta 3 = \arcsin(n \cdot \sin(\theta 1 - \theta 2)). \qquad (4)$$

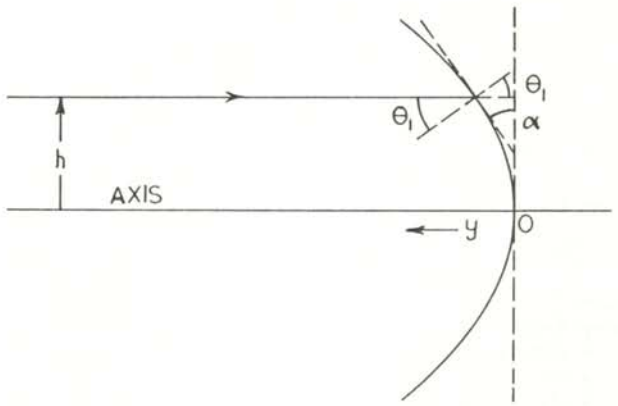

FIGURE 2
Relationship of $\theta 1$ to the slope of the parabola.

The equation of the parabolic surface of the lens is

$$y = kh^2,$$

where k is a constant and h is the ray-height. It follows then that

$$dy/dh = 2kh.$$

From the geometry of Figure 2, it can be seen that

$$\theta 1 = \alpha \quad \text{and} \quad \tan(\alpha) = dy/dh .$$

Therefore we have

$$\theta 1 = \arctan(2kh). \tag{5}$$

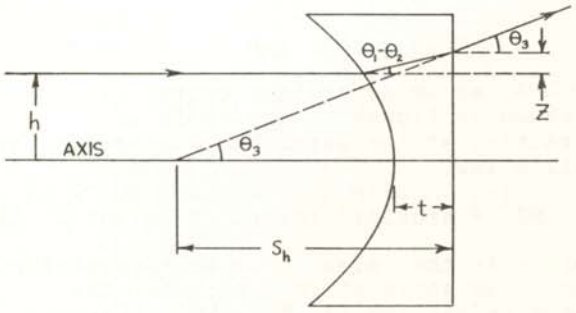

FIGURE 3
Location of the image.

To find an expression for the image distance using the geometry of the lens, one defines (see Figure 3) a distance z.

$$z = (y + t)\tan(\theta 1 - \theta 2). \tag{6}$$

We choose to measure the image distance relative to the intersection of the principal axis with the plane surface. From Figure 3, it is seen that

$$Sh = (z + h)/\tan(\theta 3) . \tag{7}$$

Substituting equations 3 through 6 into equation 7, the image distance is obtained as a function of h, k, t, and n

$$Sh = \frac{(kh^2 + t)(\tan(A-\arcsin(B))) + h}{\tan(\arcsin(n \sin(A - \arcsin(B))))} \tag{8}$$

where A = arctan(2kh) and B = (sin A)/n. It should be noted that no approximations have been made, so the result is exact.

THE EXPERIMENT

Construction of the lens

It is well known that a liquid of uniform density, rotated at constant angular velocity about a vertical axis, will have as its upper surface a paraboloid of revolution. In order to construct a permanent lens in this shape, a liquid which hardens into a transparent solid was spun in a glass cylinder mounted on a ball-bearing race. This material (2) is ordinarily used for encasing objects such as paperweights. The spinning was accomplished with a motor-driven rotator (3) whose speed could be controlled. The frequency of rotation was monitored during the catalytic hardening of the liquid using a photogate and digital timer unit (4). The parabola constant k (5) is determined by the relationship

$$k = \omega^2/(2g),$$

where ω is the angular velocity and g is the acceleration due to gravity. A desired parabola constant can be obtained by selecting the appropriate angular velocity. To accommodate the transmission of rays through the lens for large ray heights, a series of collars were poured around the original parabolic lens. These collars were made from the same substance as the original lens. The geometry of the lens is shown in Figure 4. The index of refraction of the finished lens was obtained by measuring the apparent depth of one of the collars with a microscope.

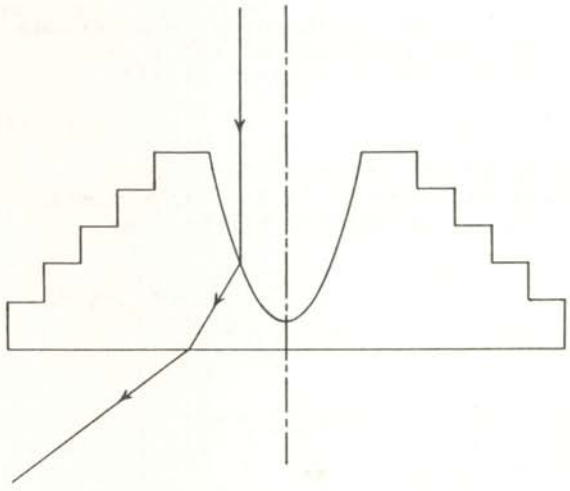

FIGURE 4
Cross-sectional view of the finished lens.

Ray Tracing

To make the ray tracing measurements, the finished lens was sawed in half along the principal axis. The sawed surface was then placed on a piece of cardboard, and a collimated laser beam was used to produce the incident rays for various ray-heights h. The center of the refracted beam was located using a screen, and the image

distances determined experimentally for a range of ray-heights.

The relevant physical properties of the finished lens were: n = 1.54, k = 0.85 (1/cm), and t = 0.90 cm. where t is the thickness of the lens.

RESULTS AND DISCUSSION

The dependence of image distance on the ray height (eqtn 8) is not trivial. A computer program was written to solve it and the results are shown in Figure 5. The LPA can then be determined by subtracting the solid curve values from the value of Sh at h = 0. It is interesting to note that the LPA is negative for small and intermediate values of h, and then becomes positive for sufficiently large values of h.

The experimental results are also shown on Figure 5. Several data points lie above the theoretical curve for small values of h. This can be qualitatively explained by noting that the actual curvature of the lens in this region was slightly less than what one would expect from the theoretical relationship between k and ω.

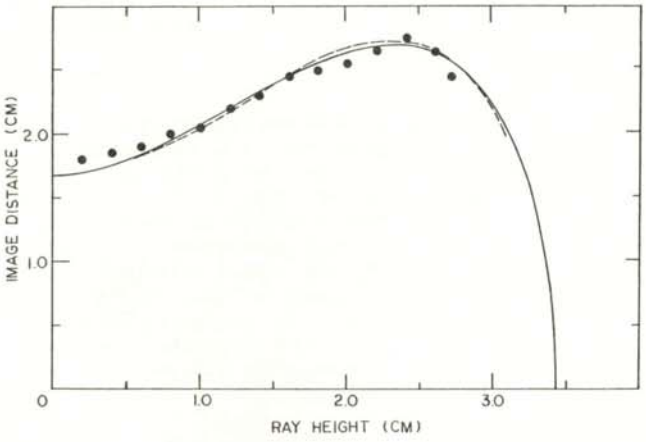

FIGURE 5
Image distance versus ray height for the finished lens. The solid curve is the exact relationship from Eqtn 8. The dots are experimental data points. The dashed curve is the approximate relationship from Eqtn 10.

The behavior of the LPA can also be interpreted by using the approach taken in understanding fifth order spherical aberrations. In this case, the LSA is approximated as

$$LSA = ah^2 + bh^4 , \quad (9)$$

where a and b are constants. Since this curve appears to have the same shape as the theoretical curve (Figure 5) for the parabolic lens, the image distance for the parabolic lens might be approximated by

$$Sh = Sp - ah^2 - bh^4 , \quad (10)$$

where a is a negative constant and b is a positive constant. Over the range of h values for which experimental data were obtained, it was found that the theoretical results could be fit to within 2% by a curve of the form of Eqtn. 10 with Sp = 1.68 cm, a = -0.40 (1/cm), and b= 0.038 ($1/cm^3$). This approximate curve is shown as a dashed line on Figure 5. Thus, the LPA of the parabolic lens may be interpreted as the sum of a negative component that dominates at small and intermediate values of h, and a positive component that dominates at larger values of h.

A final observation is that the image distance falls to zero for a ray height of approximately 3.43 cm for this lens. At this ray height, the critical angle is reached at the plane surface of the lens. The refractive behavior of rays parallel to the principal axis is described exactly by Eqtn 8 up to the point where total internal reflection occurs at the plane surface.

REFERENCES

(1) F.A. Jenkins and H.E. White, "Fundamentals of Optics", McGraw-Hill, New York, 1976, pp. 153-162.

(2) Available in hobby stores under the name "Clear Cast" and manufactured by American Handicrafts Co., Fort Worth, TX.

(3) Motor Driven Rotator, No. 74350-001, Central Scientific Co., 11222 Melrose Avenue, Franklin Park, IL 60131.

(4) Model 8015 Counter/Timer, Pasco Scientific, 1933 Republic Ave., San Leandro,m CA 94577.

(5) M.R. Spiegel, "Applied Differential Equations" , Prentice-Hall, Englewood Cliffs, NJ, 1967, pp. 118,119.

SPONSOR OF THIS PAPER
Dr. Phillip O. Berge
Physics Department
Wofford College, Spartanburg, SC 29301

LS- AND jj- COUPLED ANGULAR MOMENTUM EIGENSTATES FOR THE CONFIGURATION $(f)^7$

Harry A. Schmitt
Department of Physics
University of Denver, Denver, CO 80210

ABSTRACT

The angular momentum eigenstates for the configuration $(f)^7$ are determined in both LS- and jj-coupling for J=25/2, 23/2, and 21/2. The transformation matrices between these two representations are also constructed. Finally, the matrices are used to evaluate the matrix elements of the spin-orbit interaction in an LS-coupled system and the Landé g factors in a jj-coupled system for these states.

INTRODUCTION

In atomic spectroscopy, one analyzes various properties of the spectra of complicated atoms. In particular, the Hamiltonian for a complicated atom contains many interaction terms, which one hopes to treat as perturbations. (1),(2) If the spin-spin correlation and the electrostatic effects of the mutual electrostatic energy of the electrons dominate, we have LS-coupling. On the other hand, if the spin-orbit energy greatly exceeds the residual electrostatic and spin-spin correlation energies, we have jj-coupling. In general, light atoms tend to be mainly LS-coupled, while heavy ones tend more towards jj-coupling. One therefore needs to find the wavefunctions for equivalent electrons in both LS- and jj-coupling.

The two representations of these wavefunctions are, of course, equivalent. Using step-down operators, the creation and addition of angular momentum eigenstates is often a tedious process. It usually requires one to solve a prohibitively large number of equations. In both LS- and jj-coupling, this addition is usually easier when performed using step-up operators (3). The addition of angular momenta involves Clebsch-Gordon coefficients (4), and these are needed throughout this paper. To examine the effect of perturbations, one must obtain the matrix elements of the interactions between the unperturbed states. Often these elements are easy to evaluate in one representation, but difficult in another. It is therefore useful to construct the transformation matrices between the two representations. It should be noted that J, the total angular momentum, is a good quantum number in either coupling scheme. In the present work, we find the wavefunctions and transformation matrices for the configuration $(f)^7$ for J=25/2, 23/2, and 21/2.

In the next section, we determine the LS-coupled states in terms of LS zero-order states, followed by a section where the jj-coupled states are determined from jj zero-order states. In the next section, we use these jj- and LS-coupled states to form the jj-LS transformation matrices. In the last section, we demonstrate some of the uses of the jj-LS transformation matrices. In particular, we have calculated the matrices of the spin-orbit interaction in LS-coupling, and the Landé g factors for the jj-coupled states, for those states examined in this work.

CONSTRUCTION OF LS STATES

In the LS-representation, individual electrons are identified by the quantum numbers s, ℓ, m, m_ℓ, as well as the principal quantum number n. All electrons have spin 1/2, i.e., s=1/2. One LS representation of states is identified by the quantum numbers S, L, M_S, M_L, where L is the total orbital angular momentum and M_L, is its z component. Another LS representation is identified by the quantum numbers S, L, J, M_J, where L and S are defined as above, $\bar{J} = \bar{L} + \bar{S}$ is the total angular momentum, and M_J is the z component of J. For several particles,

$$\bar{L} = \sum_i \bar{\ell}_i \quad , \quad \bar{S} = \sum_i \bar{s}_i \quad , \text{ and } \quad \bar{J} = \sum_i \bar{j}_i$$

Let us begin work with the SLM_SM_L states. We shall denote a state of r equivalent ℓ electrons in this representation by the symbol

$$|(\ell)^r SLM_SM_L\rangle$$

or by the symbol

$$|^{2S+1}L M_S M_L\rangle$$

if the number and type of electrons are clearly understood. The top state of a system is that state which has the maximum allowable M and M for that term, i.e., M_S =S and M_L =L. If the top state is known, one can use step-down operators to obtain all the lower states of that term. If the

top state of a term exists, then all the other states associated with that term also exist. To provide a concise notation, it is convenient to introduce a shorthand notation for the Slater determinants of zero-order states. We shall denote these states by the symbol

$$|m_1^{\pm} m_2^{\pm} \ldots m_r^{\pm}\rangle$$

Where m_1 is the m_ℓ of the first electron, m_2 is that of the second, etc., and the plus or minus indicates whether the electron has a positive or negative spin component. If we now require the single particle states to appear in "dictionary order", then identical states are represented in the same way. That is, if m_1 is greater than m_2, it must precede m_2, and m_1^+ must precede m_1^-. In addition, for each position an m_i is moved, the state is multiplied by a minus one. These conventions preserve the antisymmetry and the correct sign as these states are raised or lowered by step-up or step-down operators. They also guarantee that the Pauli principle is always satisfied and that the state is completely antisymmetric under the exchange of any two electrons.

To obtain the top state of a system, one uses the methods of Reference (3). The top states of the terms that we are considering here are as follows:

where ${}^2_5N$ is the ${}^2N$ with seniority 5, and ${}^2_7N$ is the ${}^2N$ with seniority 7. We then express states identified by

$$|^{2S+1}L, J, M_J\rangle$$

as linear combinations of states identified by

$$|^{2S+1}L, M_S, M_L\rangle$$

using standard methods of vector addition.

CONSTRUCTION OF jj STATES

In jj-coupling, each electron has a particular total angular momentum j that is formed by $\bar{j} = \bar{\ell} + \bar{s}$. For f electrons, $\ell = 3$, $s = 1/2$, and therefore $j = 7/2$ or $5/2$. To build up a jj state, all of the $j = 7/2$ electrons combine to form a total J_1, and all of the $j = 5/2$ electrons combine to form a total J_2. Using standard vector addition, we add J_1 and J_2 to form a total J.

In general, if there are r equivalent electrons, n of which have angular momentum j_1 and (r-n) of which have angular momentum j_2, then the possible states are

$$\left[(j_1)^n {}_{J_1} (j_2)^{r-n} {}_{J_2}\right]$$

with n=1,2,...r. The states of $(j)^n$ which we need here are:

$$|^4N, 3/2, 10\rangle = |3^+ 3^- 2^+ 2^- 1^+ 0^+ -1^+\rangle ,$$

$$|^4M, 3/2, 9\rangle = (1/2)^{1/2}\left[|3^+ 3^- 2^+ 1^+ 1^- 0^+ -1^+\rangle + |3^+ 3^- 2^+ 2^- 1^+ 0^+ -2^+\rangle\right] ,$$

$$|^2Q, 1/2, 12\rangle = |3^+ 3^- 2^+ 2^- 1^+ 1^- 0^+\rangle ,$$

$$|^2O, 1/2, 11\rangle = (1/2)^{1/2}\left[|3^+ 3^- 2^+ 2^- 1^+ 0^+ 0^-\rangle + 3^+ 3^- 2^+ 2^- 1^+ 1^- -1^+\rangle\right] ,$$

$$\begin{aligned} |^2_5N, 1/2, 10\rangle = (1/22)^{1/2} \Big[& (6)^{1/2} |3^+ 3^- 2^+ 2^- 1^+ 1^- -2^+\rangle \\ & -(5)^{1/2} |3^+ 3^- 2^+ 2^- 1^+ 0^+ -1^-\rangle + (5)^{1/2} |3^+ 3^- 2^+ 2^- 1^- 0^+ -1^+\rangle \\ & -(6)^{1/2} |3^+ 3^- 2^+ 1^+ 1^- 0^+ 0^-\rangle \Big] , \end{aligned}$$

$$\begin{aligned} |^2_7N, 1/2, 10\rangle = (1/138)^{1/2} \Big[& 3(6)^{1/2} |3+3-2^+ 2^- 1^+ 1^- -2^+\rangle \\ & +(5)^{1/2} |3^+ 3^- 2^+ 2^- 1^+ 0^+ -1^-\rangle - 2(5)^{1/2} |3^+ 3^- 2^+ 2^- 1^+ 0^- -1^+\rangle \\ & +(5)^{1/2} |3^+ 3^- 2^+ 2^- 1^- 0^+ -1^+\rangle + 3(6)^{1/2} |3^+ 3^- 2^+ 1^+ 1^- 0^+ 0^-\rangle \Big] \end{aligned}$$

$$|(7/2)^3 15/2,15/2\rangle = |(7/2)^3 7/2,5/2,3/2\rangle ,$$

$$|(7/2)^4 8,8\rangle = |(7/2)^4 7/2,5/2,3/2,1/2\rangle ,$$

$$|(7/2)^4 6,6\rangle = (1/2)^{1/2}[\,|(7/2)^4 7/2,5/2,3/2,-3/2\rangle - |(7/2)^4 7/2,5/2,1/2,-1/2\rangle] ,$$

$$|(7/2)^5 15/2,15/2\rangle = |(7/2)^5 7/2,5/2,3/2,1/2,-1/2\rangle$$

$$|(5/2)^2 4,4\rangle = |(5/2)^2 5/2,3/2\rangle ,$$

$$|(5/2)^3 9/2,9/2\rangle = |(5/2)^3 5/2,3/2,1/2\rangle ,$$

$$|(5/2)^3 5/2,5/2\rangle = (1/2)^{1/2}\,[\,|(5/2)^3 5/2,3/2,-3/2\rangle - |(5/2)^3 5/2,1/2,-1/2\rangle] ,$$

$$|(5/2)^4 4,4\rangle = |(5/2)^4 5/2,3/2,1/2,-1/2\rangle .$$

For J=25/2, 23/2, and 21/2, the states which can be formed are:

$$[(7/2)^4_8 (5/2)^3_{9/2}]_{25/2,23/2,21/2},$$

$$[(7/2)^5_{15/2} (5/2)^2_4]_{23/2,21/2},$$

$$[(7/2)^3_{15/2} (5/2)^4_4]_{23/2,21/2},$$

$$[(7/2)^4_6 (5/2)^3_{9/2}]_{21/2},$$

and $$[(7/2)^4_8 (5/2)^3_{5/2}]_{21/2}.$$

Again, if the highest state of a system is found, then all the lower states can be obtained by using step-down operators.

As the number of states in the jj-representation must equal the number of states in the LS-representation, it must be possible to represent an LS-state as a linear combination of jj-states or vice versa. Once this linear combinaton is found, it is possible to construct one column of a jj-LS transformation matrix. These transformation matrices have some very useful properties, and their construction is the next objective of this paper.

CONSTRUCTION OF jj-LS TRANSFORMATION MATRICES

The sets of jj- and LS-states for a given J span the same space. It must therefore be possible to write any LS-state as a linear combination of jj-states. The jj-LS transformation matrices, which are independent of M , provide the "bridge" from the jj to the LS representation.

We wish to express a state

$$|(7/2)^b_{J_1} (5/2)^{r-b}_{J_2} J,J\rangle$$

as a linear combination of

$$|^{2S+1}L,J,J\rangle$$

states. We start with these states expressed as linear combinations of LS zero-order states. In general, there are more LS zero-order states than these states, so that some of the LS zero-order states will not transform independently. One, however, can select as many independent LS zero-order states as there are

$$|^{2S+1}L,J,J\rangle$$

states, and then ignore the other LS zero-order states, as they must transform as fixed linear combinations of the chosen ones. If an LS zero-order state appears only once, it must be chosen as one of the independent LS zero-order states. The next step connects the states

$$|(7/2)^b_{J_1} (5/2)^{r-b}_{J_2} J,J\rangle$$

to the states

$$|^{2S+1}L,J,J\rangle .$$

Single electron states can be specified by

$$|s,\ell\, m_s,m_\ell\rangle \text{ or } \qquad |s,\ell\,,j,m_j\rangle .$$

In both representations, ℓ and s are the same. We now wish to express the state of an electron with given j and m_j as a linear combination of states with given m_ℓ and m_s . Because these are f electrons, ℓ =3 and s=1/2; therefore j=7/2 or 5/2. Obviously for $j = m_j = 7/2$, we must have

$$|7/2\rangle = |3^+\rangle .$$

Using step-up operators, we can find the linear combination of states for $j = m_j$ =5/2. By operating on the top states with $\overline{j} = \overline{\ell} + \overline{s}$, we obtain a table of all the states of lower m_j . Here we give the top few entries for both j=7/2 and j=5/2:

j=5/2;

$$|5/2\rangle = (1/7)^{1/2}[\,|2^+\rangle - (6)^{1/2}|3^-\rangle] , \qquad (1)$$

$$|3/2\rangle = (1/7)^{1/2}[\,(2)^{1/2}|1^-\rangle - (5)^{1/2}|2^+\rangle] . \qquad (2)$$

j=7/2:

$$|7/2\rangle = |3^+\rangle \ , \tag{3}$$

$$|5/2\rangle = (1/7)^{1/2}[(6)^{1/2}|2^+\rangle + |3^-\rangle] \ , \tag{4}$$

$$|3/2\rangle = (1/7)^{1/2}[(5)^{1/2}|1^+\rangle + |2^-\rangle] \ , \tag{5}$$

Using this table and the rules of dictionary order, we can represent each jj zero-order state as a linear combination of LS zero-order states. As an example, consider the jj zero-order state

$$|7/2,5/2,3/2,1/2.-1/2\rangle\,|\,5/2,3/2),$$

in which the pointed bracket contains j=7/2 electrons and the rounded bracket contains j=5/2 electrons. This state is a linear combination of the three selected LS zero-order states

$$|3^+3^-2^+2^-1^+0^+-1^+\rangle, \ |3^+3^-2^+2^-1^+0^+0^-\rangle,$$

and $|3^+3^-2^+2^-1^+1^--1^+\rangle$.

Thus

$$|7/2,5/2,3/2,1/2,-1/2\rangle\,|\,5/2,3/2) = a|3^+3^-2^+2^-1^+0^+-1^+\rangle + b|3^+3^-2^+2^-1^+0^+0^-\rangle + c|3^+3^-2^+2^-1^+1^--1^+\rangle \ . \tag{6}$$

We now use the table to find the coefficient a; b and c are found similarly. Substituting from Equations 1 - 5 into Equation 6, we find that

$$\begin{aligned}|7/2,5/2,3/21/2-1/2\rangle\,|\,5/2,3/2) = (1/7)^3\big[&6(30)^{1/2}|3^+2^+1^+0^+-1^+\rangle|3^-2^-) \\ &-24(3)^{1/2}|3^+2^+2^-0^+-1^+\rangle|3^-1^+) \\ &+10(3)^{1/2}|3^+3^-1^+0^+-1^+\rangle|2^+2^-) \\ &+4(3)^{1/2}|3^+3^-2^-0^+-1^+\rangle|2^+1^+)\big] \ .\end{aligned}$$

Note that the use of pointed and rounded brackets is merely a bookkeeping device. After rearrangement into "dictionary order", our term becomes

$$|7/2,5/2,3/2,1/2-1/2\rangle\,|\,5/2,3/2) = -(6/7)|3^+3^-2^+2^-1^+0^+-1^+\rangle + b|3^+3^-2^+2^-1^+0^+0^-\rangle + c|3^+3^-2^+2^-1^+1^--1^+\rangle \ .$$

Because each state

$$|(7/2)^b_{J_1}(5/2)^{r-b}_{J_2}\,J,J\rangle$$

can be written as a linear combination of jj zero-order states, which can in turn be written in terms of LS zero-order states, it is possible to write it as a linear combination of LS zero-order states. As we also know the LS zero-order states in terms of

$$|^{2S+1}L,J,J\rangle$$

states, we finally obtain each jj-state in terms of LS-states. The matrix of the expansion coefficients (jj | LS) is called the jj-LS transformation matrix, For J=25/2, 23/2, and 21/2, these matrices are given in Table I. In each case, the number appearing to the right multiplies each of the matrix elements. Note that each of the matrices is orthogonal and that the equivalent LS-jj transformation matrix is therefore the transpose of the matrix given. These matrices have many uses, two of which are examined in the next section.

USES OF THE TRANSFORMATION MATRICES

The complete Hamiltonian for a complicated atom involves many terms.(5) The spin-orbit interaction which accounts for the fine structure, is introduced as a perturbation, and has the general form

$$V_{so} = -\Sigma\bar{l}_i\cdot\bar{s}_i(m^2r_ic^2)^{-1}(dV/dr) \ .$$

Because we are dealing entirely with equivalent electrons, the radial integrals will be the same for all electrons considered. The spin-orbit operator therefore reduces to

$$V_{so} = F(r)\,\Sigma\,\bar{l}_i\cdot\bar{s}_i \ ,$$

and, when we take its matrix elements between unperturbed states, the radial part integrates to a constant. We can therefore address our attention to the calculation of the matrix elements of the operator

$$\Sigma\,\bar{l}_i\cdot\bar{s}_i$$

In the jj-coupling scheme, the matrix of

$$\Sigma\,\bar{l}_i\cdot\bar{s}_i$$

is diagonal with eigenvalues

$$(1/2)\quad[j_i(j_i+1) - l(l+1) - s(s+1)]$$

For our states, the matrices of the operator

$$\left[V_{so}\right]_{jj} ,$$

are given in Table II. If we now multiply this matrix on the right by the transformation matrix and on the left by its transpose, we obtain the matrix

$$\left[V_{so}\right]_{LS} ,$$

which is the matrix of the spin-orbit interaction in the LS representation. These matrices are given in Table III.

A second example involves the calculation of the Lande g factor for a jj-coupled state. In the LS-representation, this is given by

$$g = 1 + (1/2)\left[J(J+1)+S(S+1)-L(L+1)/J(J+1)\right],$$

For our LS-states, these factors become:

$g(^2Q, 25/2)=26/25$, $g(^4N, 23/2)=26/23$,

$g(^2Q, 23/2)=24/25$, $g(^2O, 23/2)=24/23$,

$g(^4N, 21/2)=512/483$, $g(^4M, 21/2)=552/483$,

$g(^2O, 21/2)=462/483$, and $g(^2N, 21/2)=506/483$.

The g factors for the corresponding jj-states are the diagonal elements of the matrix

$$(jj|LS)(g)_{LS}\,(LS|jj),$$

which, for our states, are found to be:

$g((7/2)^4_8(5/2)^3_{9/2}, 25/2)=26/25$,

$g((7/2)^5_{15/2}(5/2)^2_4, 23/2)=24/23$,

$g((7/2)^4_8(5/2)^3_{9/2}, 23/2)=602/575$,

$g((7/2)^3_{15/2}(5/2)^4_4, 23/2)=24/23$,

$g((7/2)^4_8(5/2)^3_{5/2}, 21/2)=158/147$,

$g((7/2)^4_8(5/2)^3_{9/2}, 21/2)=170/161$,

$g((7/2)^5_{15/2}(5/2)^2_4, 21/2)=508/483$,

$g((7/2)^3_{15/2}(5/2)^4_4, 21/2)=508/483$,

and $g((7/2)^4_6(5/2)^3_{9/2}, 21/2)=50/49$.

In a magnetic field, each energy level is split as $E = e\hbar BgM/(2m)$. As e, m, $\hbar$, and B are fixed quantities, the Landé g factor determines the relative size of this splitting.

$$(7/2)^4_8(5/2)^3_{9/2}\ 25/2 \quad \begin{matrix} {}^2Q_{25/2} \end{matrix} \begin{bmatrix} -1 \end{bmatrix}$$

$$\begin{matrix} & {}^4N_{23/2} & {}^2Q_{23/2} & {}^2O_{23/2} \end{matrix}$$

$$\begin{matrix} (7/2)^5_{15/2}(5/2)^2_4\ 23/2 \\ (7/2)^4_8(5/2)^3_{9/2}\ 23/2 \\ (7/2)^3_{15/2}(5/2)^4_4\ 23/2 \end{matrix} \begin{bmatrix} -2(6)^{1/2} & 5 & -7 \\ -5(2)^{1/2} & -4(3)^{1/2} & 0 \\ -2(6)^{1/2} & 5 & 7 \end{bmatrix} (98)^{-1/2}$$

$$\begin{matrix} & {}^4N_{21/2} & {}^4M_{21/2} & {}^2O_{21/2} & {}^2{}_5N_{21/2} & {}^2{}_7N_{21/2} \end{matrix}$$

$$\begin{matrix} (7/2)^4_8(5/2)^3_{5/2}\ 21/2 \\ (7/2)^4_8(5/2)^3_{9/2}\ 21/2 \\ (7/2)^5_{15/2}(5/2)^2_4\ 21/2 \\ (7/2)^3_{15/2}(5/2)^4_4\ 21/2 \\ (7/2)^4_6(5/2)^3_{9/2}\ 21/2 \end{matrix} \begin{bmatrix} 0 & -2(330)^{1/2} & -3(46)^{1/2} & -10(15)^{1/2} & 0 \\ -14(11)^{1/2} & 0 & 0 & 0 & -7(22)^{1/2} \\ -7(11)^{1/2} & (759)^{1/2} & -12(5)^{1/2} & -(138)^{1/2} & 7(22)^{1/2} \\ -7(11)^{1/2} & -(759)^{1/2} & 12(5)^{1/2} & (138)^{1/2} & 7(22)^{1/2} \\ 0 & 6(11)^{1/2} & 2(345)^{1/2} & -27(2)^{1/2} & 0 \end{bmatrix} (3234)^{-1/2}$$

TABLE I
jj-LS Transformation Matrices

$$\left[(7/2)^4_8(5/2)^3_{9/2}\right]_{25/2} \begin{bmatrix} 0 \end{bmatrix}$$

$$\begin{matrix} \left[(7/2)^5_{15/2}(5/2)^2_4\right]_{23/2} \\ \left[(7/2)^4_8(5/2)^3_{9/2}\right]_{23/2} \\ \left[(7/2)^3_{15/2}(5/2)^4_4\right]_{23/2} \end{matrix} \begin{bmatrix} 7/2 & 0 & 0 \\ 0 & 0 & 0 \\ 0 & 0 & -7/2 \end{bmatrix}$$

$$\begin{matrix} \left[(7/2)^4_8(5/2)^3_{5/2}\right]_{21/2} \\ \left[(7/2)^4_8(5/2)^3_{9/2}\right]_{21/2} \\ \left[(7/2)^5_{15/2}(5/2)^2_4\right]_{21/2} \\ \left[(7/2)^3_{15/2}(5/2)^4_4\right]_{21/2} \\ \left[(7/2)^4_6(5/2)^3_{9/2}\right]_{21/2} \end{matrix} \begin{bmatrix} 0 & 0 & 0 & 0 & 0 \\ 0 & 0 & 0 & 0 & 0 \\ 0 & 0 & 7/2 & 0 & 0 \\ 0 & 0 & 0 & -7/2 & 0 \\ 0 & 0 & 0 & 0 & 0 \end{bmatrix}$$

TABLE II
Spin-orbit matrices in jj-coupling

CONCLUSIONS

The techniques used to obtain the eigenstates and transformation matrices for J=25/2, 23/2, 21/2 can be used equally well for lower values of J, although the work increases rapidly. If we use Hund's rule to order the energies of the states of atoms in the configuration $(f)^7$, we see that the ground state is $^8S_{7/2}$. The values of J for which we have obtained matrices are obviously far from those of

$$^2O_{25/2}\ [0]$$

$$\begin{array}{l} {}^4N_{23/2} \\ {}^2O_{23/2} \\ {}^2O_{23/2} \end{array} \begin{bmatrix} 0 & 0 & 2(6)^{1/2} \\ 0 & 0 & -5 \\ 2(6)^{1/2} & -5 & 0 \end{bmatrix} (2)^{-1/2}$$

$$\begin{array}{l} {}^4N_{21/2} \\ {}^4M_{21/2} \\ {}^2O_{21/2} \\ {}^2{}_5N_{21/2} \\ {}^2{}_7N_{21/2} \end{array} \begin{bmatrix} 0 & -(253)^{1/2} & 4(15)^{1/2} & (46)^{1/2} & 0 \\ -(253)^{1/2} & 0 & 0 & 0 & (506)^{1/2} \\ 4(15)^{1/2} & 0 & 0 & 0 & -4(30)^{1/2} \\ (46)^{1/2} & 0 & 0 & 0 & -2(23)^{1/2} \\ 0 & (506)^{1/2} & -4(30)^{1/2} & -2(23)^{1/2} & 0 \end{bmatrix} (132)^{-1/2}$$

TABLE III
Spin-orbit matrices in LS-coupling

the low-lying terms of this configuration. As these lower terms are the ones mainly observed, they are necessary in the spectral analysis of such an atom. In this sense, we have only begun the problem.

Once we have found the transformation matrices, they can be used to find the matrix elements of many different perturbations is both LS- and JJ-represenations. A list of different perturbations to be considered can be found in any standard reference dealing with atomic spectroscopy. (6) As one reaches smaller J values, the size of the transformation matrices greatly increases; however, the techniques outlined in this work can be used to construct these larger matrices.

The main purpose of this paper has been to gain insight into the methods of the construction and analysis of angular momentum eigenstates, as well as an understanding of spectroscopic phenomena. We have begun this work on the configuration $(f)^7$ which characterizes the ground states of Eu, Gd, Am, and Cm. Continuation of this work will complete the analysis of this configuration. Once similar work is carried out on the remaining configurations of the f shell, it will be possible to make systematic studies of the spectra of both the rare earth and the radioactive actinide series.

ACKNOWLEDGMENTS

The author wishes to thank Dr. E.R. Tuttle for advice and assistance during the progress of this work. He would also like to thank Ms. Armour-Hileman for her help in the editing and revision of this manuscript. The work was supported in part by the Honors Program of the University of Denver.

REFERENCES

(1) E.U. Condon and G.H. Shortley, "The Theory of Atomic Spectra", Cambridge University, Cambridge, 1963, pp. 159-160.

(2) R.B. Leighton, "Principles of Modern Physics", McGraw-Hill, New York, 1959, pp. 256-257.

(3) E.R. Tuttle, Am. J. Phys. 49, 165 (1981).

(4) A. Messiah, "Quantum Mechanics", Wiley, New York, 1964, Vol. II, pp 560-563.

(5) A typical list is given in, e.g., R.B. Leighton, op. cit., pp. 256-357.

(6) E.U. Condon and G.H. Shortley, op. cit.

SPONSOR OF THIS PAPER
Dr. E.R. Tuttle
Department of Physics
University of Denver, Denver, CO 80208

THE ELECTRONIC CONTROLS USED IN A SEARCH FOR FRACTIONAL CHARGES IN MERCURY DROPS *

F. Wm. Walters, D.C. Joyce, P.C. Abrams, K.R. Coburn, B.A. Young
Physics and Astronomy Department
San Francisco State University, San Francisco, CA 94132

ABSTRACT

At San Francisco State University, we have developed an Automatic Millikan Device (AMD) for measuring the charge on small drops of Mercury. The device uses a standard atomic physics laboratory Millikan chamber, a piezoelectric driven ink-jet glass dropper, and a laser-photomultiplier system for tracking the motion of the drop. This paper describes the electronic control and error detection system used with the AMD. Signals from this system are sent to a microprocessor which controls the experiment. To this date (Dec 7, 1981), we have measured 175 micrograms of Hg and found no fractional charges in 1.05×10^{20} nucleons.

INTRODUCTION

Zweig and Gell-Mann (1) postulated in 1964 the existence of fractionally charged Quarks as the primary constituents of hardons. Since that time, there have been many searchs for free fractional charges. (2) To date, the various searches have produced either negative or at best, dubious results, with one exception: the Stanford experiments of Phillips, LaRue, Fairbank, and Hebard. (3) In the Stanford experiment, a superconducting Niobium sphere is levitated in a magneic field, and the charge is measured by varying the electric field and observing the motion of the sphere with a Squid (a sensitive magnetic field detector). Roughly one-third of the 90 microgram spheres measured showed fractional charges. Morpurgo and Marinelli (4) used a "Magnetic Levitaton Electrometer" to levitate steel spheres and found no fractional charge in the samples they measured. None of the studies to date have proven conclusively the existence or non-existence of free fractional charges. In 1978, our group decided to build an Automated Millikan Device (AMD) to measure the charges on drops of fluids injected into a Millikan device (6).

GENERAL OVERVIEW OF THE EXPERIMENT

The AMD (see Figure 1), in operation for over a year and a half, can measure the charge on up to 45 micrograms of Mercury per day. The light from the Argon laser illuminates drops of Mercury which are ejected from a glass dropper (7) into the region between two parallel capacitor plates spaced about 0.5 cm. apart. The drops are injected between the plates at a rate of close to 0.7 Hz. The laser light, scattered by the falling drops, passes through a side window and is focussed onto a series of 92 slits by a telescope. The light passing through the slits is monitored by three photomultiplier tubes. The signals from the tubes are used to check for error conditions and to determine the velocity at which the drop is falling. As the small sphere of Mercury drops, the voltage on the plates is changed three times in order to determine the charge on the drop.

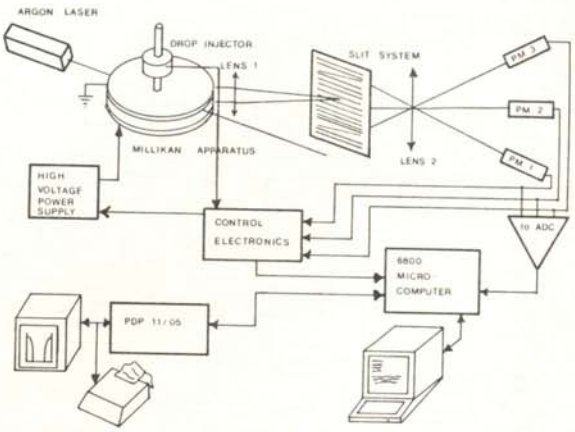

Figure 1
A general overview of the Automated Millikan Device.

The slit system is a glass photographic mask with ninety-two 100 μm wide slits which was made by an integrated circuit photoetching process at Stanford University (8). Phototubes one and three (PM 1 and PM 3) see the first set of two slits and the last set of two slits. These slits are guards for error conditions such as multiple drops in the region between the plates. The remaining central 88 slits are seen by phototube two (PM 2). The first and last of these slits

are slightly diagonal and can be used with timing measurements to check for horizontal motions of the drop. The remaining center-most 86 slits are horizontal and parallel to each other. They are used to measure the velocity of the drop.

The signals from the photomultipliers go to an electronic control system which determines the switching time for the high voltage on the bottom plate of the AMD, checks for error conditions, and combines the three signals for analog-to-digital conversion and analysis by the microcomputer. The computer then calculates the drop's velocity in the three regions of different voltage. From this information, the drop's radius, mass, and charge (as well as change in charge) are determined.(6) A hardware error condition or an error discovered in analysis will cause the rejection of the event. If there are no error conditions, the computer stores the values of charge, radius, and the change in charge in its

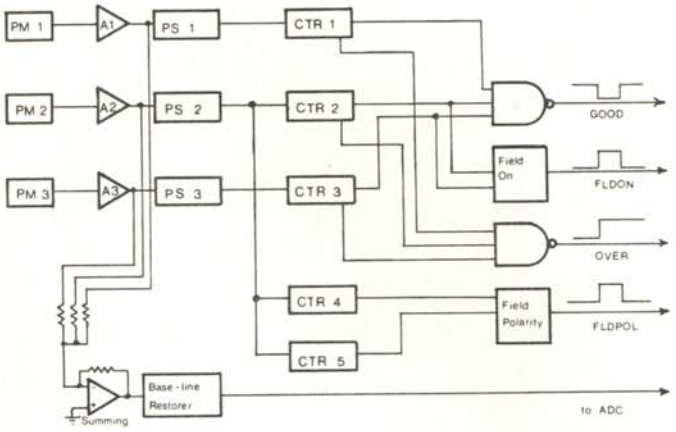

Figure 2
The control electronics. The block diagram includes the photomultiplier tubes (PM), their amplifiers (A), counters (CTR), and the peak-squarers (PS)

memory. After a run of up to four-thousand good events has occured, the data stored in the microcomputer is transferred to the PDP 11/05 for final analysis of the run.

CONTROL ELECTRONICS AND SUMMING CIRCUIT

The control electronics (Figure 2) generate various output signals that are sent to the microcomputer and are used to determine if an event is good or bad. As the image of the drop moves across the slit system, the phototubes send an output pulse whenever the scattered laser light falls on the transparent part of the slit. The signals from the photomultipliers are inverted, amplified, and conditioned in a series of peak-squarers. The three counters (CTR 1, CTR 2, CTR 3) count the pulses from their corresponding photomultiplier tube. Logic circuits are used to determine if the correct number of signals were sent by each phototube: two from the first, 88 from the central tube, and 2 more from the last tube. If each of the counters indicate the correct number

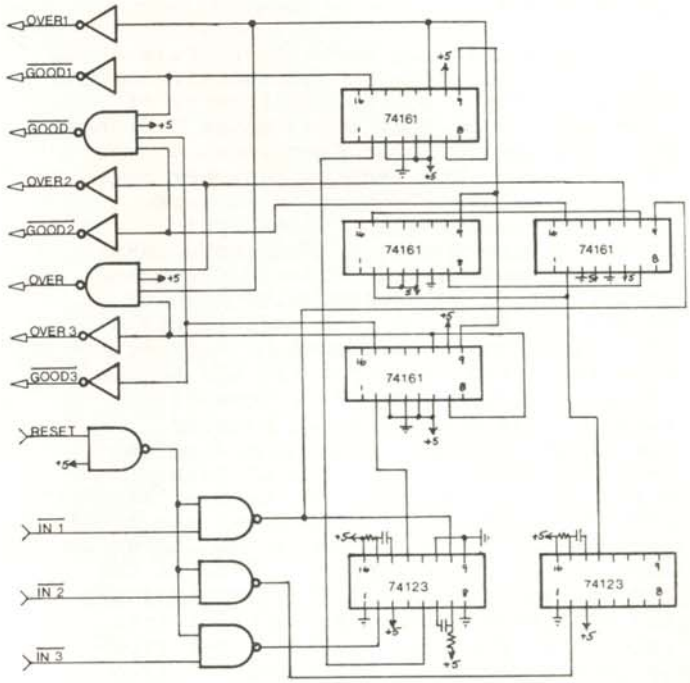

Figure 3
The error detection circuit consists of two 4-bit counters (CTR 1 and CTR 3) and an 8-bit counter (CTR 2). The 74123's are monostable multivibrators used to condition the signals as the come into they counter circuit.

of pulses, a $\overline{\text{GOOD}}$ (the level rests high and when the condition is met, it drops to low) is sent to the computer. The signal from PM 2 (which monitors the middle 88 slits) controls when and what polarity high voltage is placed on the bottom plate

of the AMD. A correct count in CTR 4 sets a flip-flop (FLDPOL) that controls the field polarity between the plates. A correct count in CTR 5 clears FLDPOL. If any of the counters over-count, an OVER signal is sent to the front panel for display purposes and to the field-on (FLDON) circuit to cut off the voltage on the bottom plate.

While the counters in the control electronics are checking for errors in the number of peaks detected, a summing circuit combines the signals from the three photomultiplier tubes. This signal goes through a base-line restorer which maintains the output base line at ground. This signal is then sent to an analog-to-digital converter in the microprocessor. The digitized signal from the photomultiplier tubes is used to caluclate the speed at which the drops are traveling. This information, coupled with the size of the electric field, allows the computer to calculate the charge on the drop.

Signal conditioning circuits

The signal from each of the photomultiplier tubes is sent to a peak-squarer (Figure 3) to be converted into a square pulse for counting. The first op-amp acts as an AC-coupled buffer amplifier which couples the signal to a false ground of 2.5 volts. The second op-amp is used as Schmitt trigger with a variable threshold. After the peak-squarers, the signals are further conditioned by a 74123 monostable

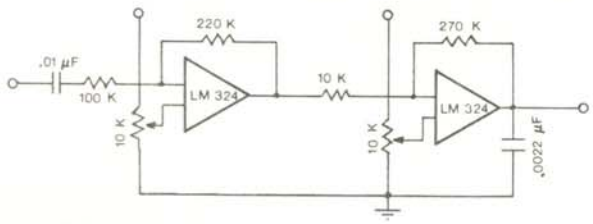

Figure 4
The peak-squarer circuit contains 2 op-amps. The first is used as a buffered input and the other as a Schmitt trigger. Both op-amps have a small gain to condition the signal for input to the counters.

multivibrator. This sets the proper length to the digital signal needed for input into the counters.

Error detection circuit

CTR 1, CTR 2, and CTR 3 in the error detection circuit (Figure 3) are used to search for error conditions that can arise from a number of sources. CTR 1 and CTR 3 are 4-bit binary counters (74161 chips) and CTR 2 is an 8-bit binary counter (two 74161 chips in series). The counters are initialized by a reset pulse generated when the dropper is pulsed to inject a drop in the chamber. This reset pulse loads a predetermined number into the counters: 13 for CTR 1 and CTR 3, and 167 for CTR 2. When two pulses are counted by CTR 1 or CTR 3, or 88 pulses by CTR 2, the overflow pin in the counter will go high and the most significant bit of the counters will go low. This is the signal that the counter received the correct number of counts. The $\overline{\text{GOOD}}$ signal is generated by putting the three overflow signals through a 3 input NAND gate. The signal that indicates that the counter had over-counted is generated by examining the overflow pin the the most signifcant bit. If both go low, the OVER goes high and $\overline{\text{GOOD}}$ remains high. If any counter under-counts, the overflow pin remains low ($\overline{\text{GOOD}}$ is high) and the most significant bit remains high (OVER is low). There is a $\overline{\text{GOOD}}$ and OVER for each counter.

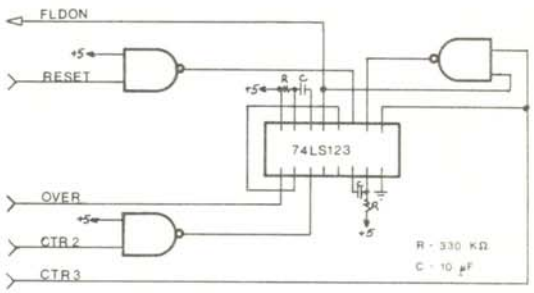

Figure 5
The FLDON circuit shown above is cleared by a reset pulse which is generated at the beginning of each event. The FLDON signal goes high when a pulse from PM 2 is received through IN 2. The electric field remains on until either the signal from PM 2 stops coming in, or the signal from PM 3 is received.

High voltage control circuits

The FLDON and FLDPOL circuits for the high voltage are controlled by the signal from PM 2. When the image of the drop reaches the third slit, the voltage on the bottom plate is set to +10,000 V. The drop then falls past 39 horizontal slits, and when the drop reaches the 40th slit, the

field polarity is reversed to -10,000 V. After passing 34 more slits, the field polarity is again changed to +10,000 V for the final 14 slits. The electric field takes a few milliseconds to stabilize during each switch. The micropocessor can check for changes in the charge of the drop, since the drop velocity must be the same in the same electric field.

The FLDON (Figure 5) signal to the high voltage supply is controlled by a TTL 74123 chip. As long as the signal from PM 2 is coming in, and the OVER pulse is not received, FLDON remains high. When the signal from PM 2 is no longer received, FLDON goes low after 1/2 second. When the signal from PM 3 starts to come in,

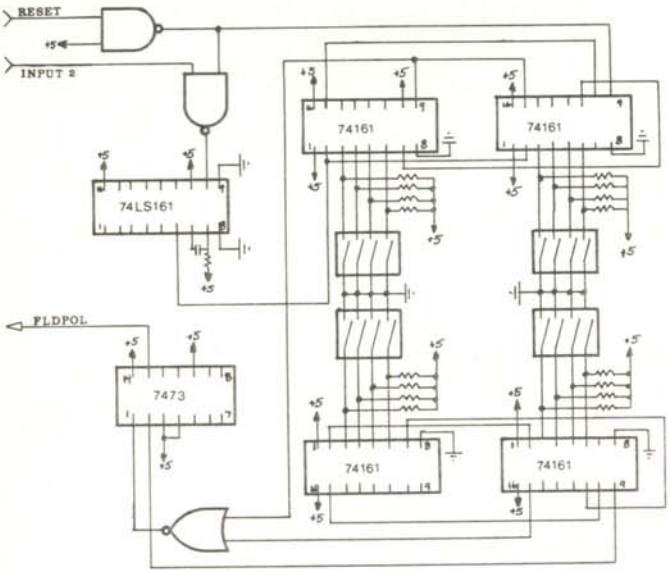

Figure 6
The FLDPOL counters (CTR 4 and CTR 5) generate the signals that control the reversal of the electric field. CTR 4 controls the first reversal, and CTR 5 controls the second one.

flip-flop B goes low, clearing flip-flop A and FLDON goes low, turning off the high voltage on the bottom plate of the AMD.

The FLDPOL circuit (Figure 6) is controlled by CTR 4 and CTR 5 which count the pulses from PM 2. The number of pulses between each reversal of the field is controlled by two sets of eight DIP switches, set to 215 and 180 respectively. The FLDPOL flip-flop (a 7473 chip) is set by the overflow pulse from CTR 4 for the first reversal and cleared by the overflow pulse from CRT 5 for the second reversal.

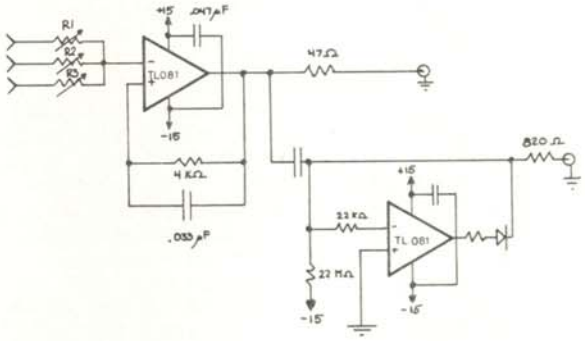

Figure 7
The summing circuit and base line restorer. This signal is sent to the ADC in the microprocessor to determine the speed of the falling drop.

The three signals from the photomultiplier tubes are added together using a TL081 op-amp (Figure 7). The amplitudes of the input signals from the tubes are individually controlled by varying the resistors R1, R2, and R3. The output from ths summing circuit goes to a Tektronix 2600 plug-in module and to the base-line restorer. This pulse is then sent to the microprocessor to calcuate the velocity and hence the charge on the drop.

RESULTS

We have measured (as of December 7, 1981) a total of 175 micrograms of Mercury. 60 micrograms were triply distilled lab Mercury and 115 micrograms were native Mercury (unpurified) from the Socrates Mine in Northern California. Figures 8 and 9 show data from different evolutionary states of the experiment. These histograms show the residual charge, the charge remaining after the integer part is subtracted, vs the number of drops of Mercury detected. Figure 8 shows data from earlier runs, where charge changes were rejected only if the change in charge on the drop was in the range between 0.25 and 0.75 electron charges. The statistical tails on the integral-charge peaks probably are due to charge changes. Figure 9 shows runs where all charge changes were rejected as bad events.

Our experiment has measured the largest sample of Mercury (175 micrograms) and of any element heavier than Niobium on the periodic table. We follow the Morpurgo et. al. experiment which examined 3.4 milligrams, and the Fairbank et. al. experiment which used 1.2 milligrams. We found no fractional charges in the 175 micrograms of Mercury measured to date. This sets an upper limit on the concentration of fractionally charges at 1 in 1.05 x 10^{20} nucleons.

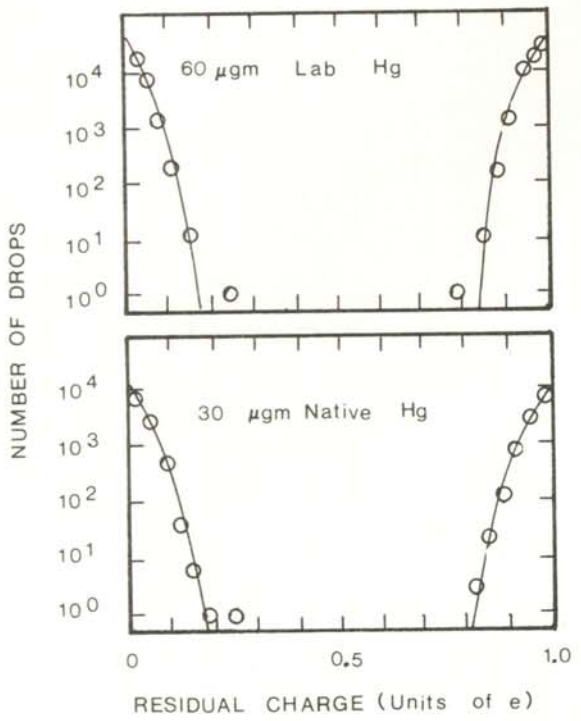

Figure 8
The first results of the search. These data include events where the charge changed on the drop.

REFERENCES

* This work was supported in part by grants from the Research Corporation of American and DOE grant #DE-AC03-81ER40009.

(1) G. Zweig, CERN Report TH-412 (1964), and M. Gell-Mann, Phys. Lett. 8, 214 (1964).

(2) L. Loyons, "Current Status of Quark Searches", Oxford University, 1980.

(3) G.S. LaRue, Wm. Fairbank, and A.F. Hebard, Phys. Rev. Let. 38, 1011 (1977), and G.S. LaRue, Wm. Fairbank, and J.D. Phillis, Phys. Rev. Let., 142, 1019 (E) (1979).

(4) M. Marinelli and G. Morpurgo, Phys. Rev. Let. 94B, #3, 427.

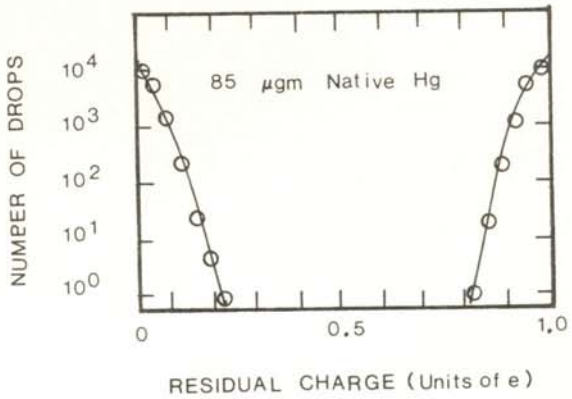

Figure 9
The latest results (as of Dec 7, 1981). In this sample of native Mercury, we detected no fractionally charged drops. In these events, we rejected any runs where the charge on the drop changed.

(5) R.W. Bland, D. Bocobo, M. Eubank, J. Royer, Phys. Rev Let., 39, 369 (1977).

(6) R.W. Bland, C.L. Hodges, P. Abrams, A.R. Baden, D.C. Joyce, J.P. Royer, F.Wm. Walters, P.G.Y. Wong, K.C. Young, B.A.Young, E.G. Willson, Phys. Rev. Let. 47, 1651 (1981).

(7) Developed by D.C. Joyce and C.L. Hodges and described in unpublished report QS-2, "Automatic 5 Micron Drop Production".

(8) Obtained for us by E.G. Wilson.

(9) F.Wm. Walter, Electronics for the Automated Millikan Quark Detector", unpublished.

SPONSOR FOR THIS PAPER
Dr. Roger Bland
Physics and Astronomy Department
San Francisco State University,
San Francisco, CA 94132